Journal of Materials Science: Materials in Medicine (2020) 31:42
https://doi.org/10.1007/s10856-020-06383-9

BIOMATERIALS SYNTHESIS AND CHARACTERIZATION

Original Research

Degradation, wettability and surface characteristics of laser surface modified Mg–Zn–Gd–Nd alloy

Rakesh K.R.[1,2] · Srikanth Bontha[1] · Ramesh M.R.[1] · Mitun Das[3] · Vamsi Krishna Balla[3,4]

Received: 20 November 2019 / Accepted: 13 April 2020 / Published online: 29 April 2020
© Springer Science+Business Media, LLC, part of Springer Nature 2020

Abstract

This work evaluates the effects of laser surface modification on Mg–Zn–Gd–Nd alloy which is a potential biodegradable material for temporary bone implant applications. The laser surface melted (LSM) samples were investigated for microstructure, wettability, surface hardness and in vitro degradation. The microstructural study was carried out using scanning and transmission electron microscopes (SEM, TEM) and the phases present were analyzed using X-ray diffraction. The in vitro degradation behaviour was assessed in hank's balanced salt solution (HBSS) by immersion corrosion technique and the effect of LSM process parameters on the wettability was analyzed through contact angle measurements. The microstructural examination showed remarkable grain refinement as well as uniform redistribution of intermetallic phases throughout the matrix after LSM. These microstructural changes increased the hardness of LSM samples with an increase in energy density. The wetting behaviour of processed samples showed hydrophilic nature when processed at lower (12.5 and 17.5 J/mm^2) and intermediate energy density (22.5 and 25 J/mm^2), which can potentially improve cell-materials interaction. The corrosion rate of as cast Mg–Zn–Gd–Nd alloy decreased by ~83% due to LSM.

Graphical Abstract

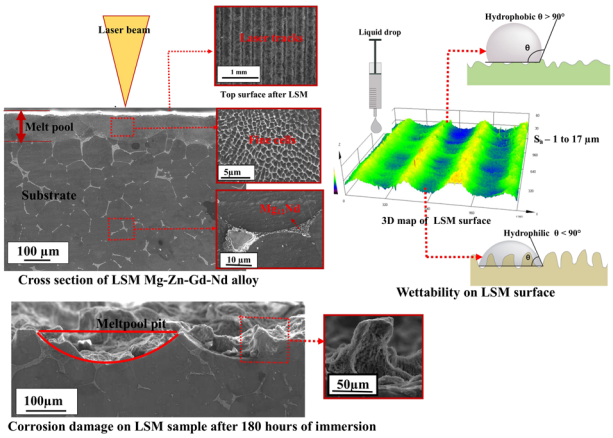

✉ Srikanth Bontha
srikanth.bontha@nitk.edu.in

✉ Vamsi Krishna Balla
vamsiballa@cgcri.res.in

1 Department of Mechanical Engineering, National Institute of Technology Karnataka, Surathkal 575025, India

2 HMT Machine Tools Ltd, Kalamassery 683503, India

3 Bioceramics and Coating Division, CSIR-Central Glass and Ceramic Research Institute, 196 Raja S.C. Mullick Road, Kolkata, West Bengal 700 032, India

4 Material Innovation Guild, Department of Mechanical Engineering, University of Louisville, Louisville, KY 40208, USA

1 Introduction

The evolution of magnesium (Mg) alloys as biodegradable materials are because of their good biocompatibility and adequate mechanical properties [1]. In order to attain an optimum combination of properties, it is important to design new Mg-based alloys or carry out surface modification of the existing alloys. In depth studies have been carried out on selecting the appropriate alloying elements and tailoring properties by altering their microstructure [2, 3]. The addition of rare earth elements (REE's) as alloying elements are shown to have a beneficial effect on the mechanical and corrosion properties of Mg. Further, Zirconium (Zr) is usually added to Mg alloyed with REE's to both refine the grain size as well as to improve the corrosion resistance [4]. The short term effect of various REE's (i.e., Gadolinium (Gd), Dysprosium (Dy), Neodymium (Nd), Yttrium (Y), Lanthanum (La), Cerium (Ce), Europium (Eu) and Zirconium (Zr)) were evaluated for cytotoxicity study on primary cells and cell line [5]. The results showed that out of all these REE's, high soluble Gd and low soluble Nd were considered as better alloying elements for biodegradable Mg alloys. Zinc (Zn) is also a nutritional element in the human body and the addition of Zn in a smaller percentage (1 wt%) increases the strength of Mg by solid solution strengthening [6]. Recently developed Mg–Nd–Zn–Zr (JDBM) alloy has proven to be an ideal material for biomedical applications due to its low corrosion rate (0.28 mm/year) [7]. Further, corrosion and mechanical properties of this alloy are improved by coating (brushite) [8] and secondary deformation (extrusion) techniques [9].

An appropriate surface modification technique can tailor the near-surface properties such as microstructure, hardness and elemental distribution. These changes directly influence the corrosion resistance and bioactivity properties of the material system. Among various surface modification techniques, the use of laser energy to alter the surface has shown to be a promising approach [10–12]. This is because laser surface modification causes a significant change in microstructure and surface properties. In Laser Surface Melting (LSM) which is a surface modification technique, a high-intensity laser beam is applied to melt the surface of materials. Due to the instant rapid heating and resolidification caused by LSM, combined effects of homogenization, refinement of grains and dissolution of the secondary phases [13] with extended solid solubility [14] have been observed. Abbas et.al., [15] studied laser surface melting of AZ31, AZ61 and WE43 alloys with a 2 kW continuous-wave laser beam. They reported an improvement of 30%, 66% and 87% improvement in corrosion resistance for AZ31, AZ61 and WE43 alloys, respectively. This was attributed to the refinement of the microstructure and uniform distribution of corrosion-resistant phases. Similarly, laser surface melting treatment (LSMT) on ZE41 alloy resulted in a homogenous distribution of alloying elements and improved hardness (170%) and corrosion resistance [14]. LSM using an excimer laser on AZ91D [16] alloys showed that the localized corrosion significantly reduced with lower i_{corr} and good passive region. Similarly, LSM of WE43 alloy using excimer laser, showed lower corrosion current in anodic and cathodic regions indicating a higher corrosion resistance than untreated samples [14].

Rakesh et al. studied LSM of Mg–Zn–Gd and Mg–Zn–Dy alloy for biomedical applications [17, 18]. This study reported that samples processed at higher energy density conditions exhibited better corrosion resistance in Hank's Balanced Salt Solution (HBSS). This study also reports enhanced wettability which is suitable for cell adhesion. Wettability (hydrophilic/hydrophobic), roughness and surface energy were also found to be critical parameters that effect the biological response between bone and implant interface [19]. In a study on laser surface modified Ti–6Al–4V alloy, it was reported that the surface with increased roughness improved the bone cell adherence and proliferation [20]. Different surface structuring on AZ31B alloy by a laser source showed suitable control of contact angle (water) with respect to surface roughness [21].

The present study focuses on laser surface modification of cast Mg–Zn–Gd–Nd alloy. LSM was carried out on the alloy at different laser processing conditions. The effect of laser energy density on microstructure, hardness, wettability and degradation characteristics are systematically investigated in this work.

2 Materials and methods

2.1 Casting of alloy

Mg–3 wt%Zn–1.5 wt%Gd–1.5 wt%Nd alloy was developed by conventional casting route. The alloying elements, neodymium (Nd) and gadolinium (Gd) of 99.9% purity were added slowly to Mg–Zn melt at a melting temperature of 750 °C. Further, a small amount of zirconium (Zr = 1 wt%) was added to the molten pool for grain refinement. The complete dissolution of the alloying elements in the melt was carried out by mechanical stirring. The stirred melt was then transferred into a preheated (250 °C) cast iron mould (200 mm × 110 mm × 20 mm). The cast alloy was analyzed using Atomic Emission Spectroscopy (ICP-AES) (IRIS INTREPID II XSP DUO, Thermo Electron) and the obtained composition is 3.01 wt% of Zn, 1.5 wt% Nd, 1.6 wt% Gd and 1 wt% Zr as reported in a prior work of the authors [22].

2.2 Laser surface melting

The Mg–Zn–Gd–Nd alloy block was cut into 100 × 30 × 8 mm alloy strips for laser surface melting (LSM). The alloys strips were then carefully polished by SiC grit polishing paper. Finely polished samples were loaded to the LENS™ machine (MR7-Optomech, Inc USA). The glove box of the machine is purged with argon gas with an oxygen level of less than 10 ppm. Ytterbium doped fibre laser was used in this LENS™ system to melt the surface of the alloy. The operating parameters such as laser power and velocity were chosen to obtain appropriate energy densities. The depiction of the laser process parameters in terms of energy density was calculated by using the following formula [23].

$$E = P/\nu.d, \quad (1)$$

where P is laser power (W), ν is scan velocity (mm/s), and d is laser beam diameter (500 µm). The distance between two consecutive laser scans is 0.5 mm

2.3 Characterization of the alloy

The cross-sectional morphology and melt pool depth were observed by using a field emission scanning electron microscope (CARL ZEISS, FESEM, Germany). The chemical composition of the prepared alloy was determined by using energy dispersive spectroscopy (EDS) attached with the FESEM. Transmission electron microscope (JEOL, model JEM-2100, operating at 200 kV) was used to understand the eutectic structure of developed Mg–Zn–Gd–Nd alloy. For TEM studies, the specimen was initially sliced to 1 mm thickness by using a slow speed precision cutting machine. The thickness was controlled from either the top surface or from both sides of the sample by mechanical thinning. The mechanical thinning is followed by dimpling and ion milling (PIPS, GATAN, USA) to further reduce the sample thickness.

The phase analysis was performed by using Glancing Incident X-ray Diffractometer (GIXRD) (Rigaku smart lab, Japan), using Cu-Kα radiation of wavelength 0.154 nm with a step size of 0.02° and a scan speed of 2° per minute. Data was recorded over the diffracting angle 2θ ranging from 20° to 80°.

Vickers micro-hardness test was carried out by using a micro-hardness tester (HMV-G20 Shimadzu, Japan) with a load of 25 g for a dwelling time of 15 s. Each measurement value represents an average value of 10 individual measurements.

2.4 Roughness and wettability analysis of LSM alloys

The surface roughness of LSM samples was studied by non-contact laser profilometer (OLYMPUS-LEXT 3D laser measuring microscope, OLS4000, Japan). The parameters S_q (root mean square height, µm) and S_q (Arithmetic mean height, µm) can be estimated from the surface topography. The data is collected over an area of 1 cm^2 of LSM sample. For extracting reliable results for biomedical applications, the effect of laser energy on both uneven as well as polished surfaces was analyzed.

The contact angle was measured by the sessile drop method with a contact angle goniometer. Deionized (DI) water (polar) and diiodomethane (non-polar liquid) were used as the medium to study the wettability of LSM samples. Initially, the polished and unpolished LSM samples were pre-cleaned by ultra-sonication in isopropyl alcohol. Then, a 1 µL droplet of liquid was dropped on the LSM sample surface using a syringe and drop formation was captured with a high-resolution camera. The surface energy of LSM samples was calculated using the Fowkes equation [24].

2.5 In vitro degradation

LSM samples with 1 cm^2 area were used for static immersion corrosion studies. The LSM surface is finely polished with 2000 grade sheet followed by velvet cloth polishing with 0.5 µm diamond paste to avoid the surface roughness effect on corrosion. The samples were appropriately mounted in epoxy resin. The exposed surface is cleaned with distilled water and toluene. Hank's balanced salt solution (HBSS, HIMEDIA, Bangalore, India) of 300 ml was used on each sample for the immersion study. The samples were exposed to the solution for a time of 180 h. The rates of hydrogen evolution and Mg^{2+} concentration were monitored for every 24 h of immersion. The apparatus used for this study is analogous to the ones used in the literature [25] for immersion corrosion studies. The Mg^{2+} ion concentration from the collected samples was measured by using Atomic Absorption Spectroscopy (932-Plus, GBC Scientific Equipment Ltd, Australia). After the completion of the immersion studies, the corrosion products formed on the samples were carefully collected. Further, the samples were cleaned in chromic acid for 10 min to remove deposited corrosion products and then washed with distilled water followed by air drying.

The corrosion rate from the hydrogen evolution was estimated by the following relation [26–28].

$$P_w = 3.65\Delta W/\rho. \quad (2)$$

P_w is the average corrosion rate in mm/year, ΔW is the weight loss rate of the sample in mg/cm^2/day and ρ is the density of the alloy (1.768 g/cm^3).

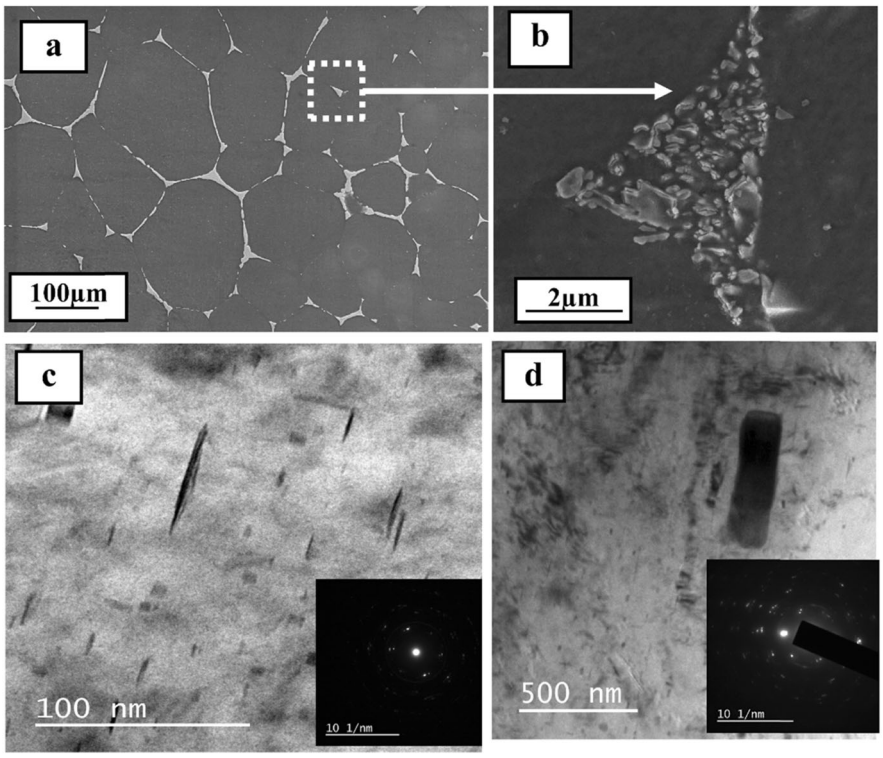

Fig. 1 SEM Morphology of **a** as-cast alloy **b** secondary phases at the grain boundary (enlarged), TEM micrograph of **c** granular particles and **d** rod shaped particles

The hydrogen emission rate V_H (ml/cm^2/day) is related to ΔW (mg/cm^2/day) using the following relation

$$\Delta W = 1.085 V_H. \quad (3)$$

Corrosion rate (mm/year) was calculated by substitution of ΔW obtained from Eq. (3) in Eq. (2).

The cleaned samples were weighed by using a four-digit precision weighing balance and corrosion rates were found out by using the following equation as given in ASTM-G31-72 [29, 30].

$$CR = \frac{K.W}{D.A.T}, \quad (4)$$

where CR is the corrosion rate in mm/year (mmpy), K is a constant (8.76×10^4 mm per year), W is the difference between the initial and the final mass of the sample, A is the area which is exposed in cm^2, D is the density of the material in g/cm^{3}and T is the total immersion time (180) in hours.

The corrosion products were analyzed using SEM, EDS and XRD to understand the morphology and contents of the precipitates. Further, to identify the functional group present in the corrosion products, FTIR spectroscopy (Jasco FTIR-4200, Japan) was carried out. The scratched out corrosion products from the immersion study samples were suitably mixed with potassium bromide and then pressed into a round disk shape (transparent). The acquisition was carried out in the wavelength range of 4000–400 cm^{-1} using KBr pellet method.

3 Results and discussion

3.1 Microstructural analysis

The preliminary investigation on the microstructure of the LSM Mg–Zn–Gd–Nd alloy was carried out using SEM and TEM techniques, and the micrographs are shown in Fig. 1. The SEM of the as-cast alloy showed the formation of large equiaxed dendritic α grains with secondary phases that surrounds the α-phase (dark grey) (Fig. 1b) in the semi-continuous network. The secondary phases were identified as $Mg_{12}Nd$ (Fig. 1b), and it was also reported in [22]. The average grain size of the as-cast sample is in the range of 60–130 µm which indicates the low cooling rate during the casting process. The specific distribution of phases is observed in the grain triple points that are reported as T-phase [31] appearing as a white network in Fig. 1a. An enlarged view of this phase is shown in Fig. 1b. TEM analysis was carried out on the as cast alloy to observe the detailed distribution of phases. Figure 1c, d shows the bright-field TEM images with selected area SAED patterns. Granular (Fig. 1c) and rod-shaped (Fig. 1d) precipitates were observed in the matrix and grain boundaries. The sizes of the precipitates were in the range of 20–500 nm. The identified granular phases are mainly Mg_7Zn_3 and this kind of similar morphology was reported in [32].

The as-cast Mg–Zn-Gd–Nd alloy surface was melted at different laser energy densities. The cross-sectional SEM

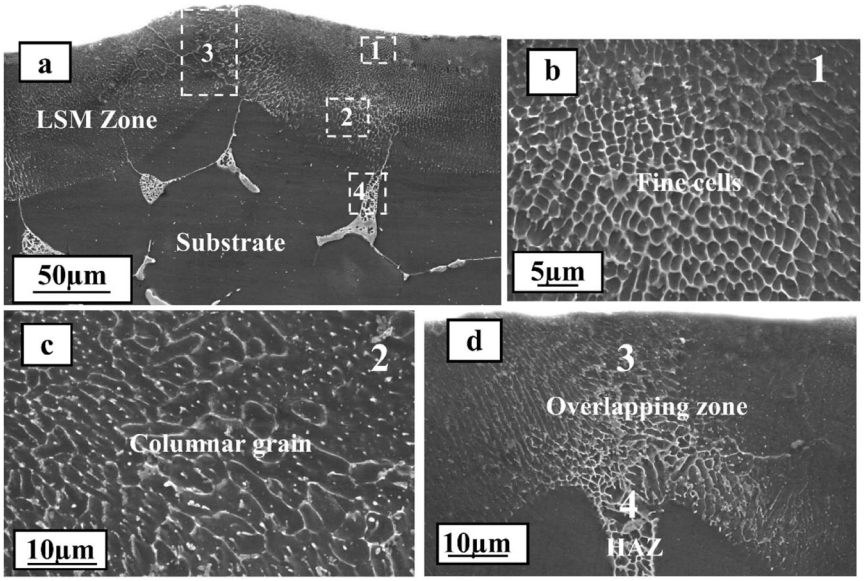

Fig. 2 Cross-sectional SEM morphology of LSM samples processed at 35 J/mm^2

micrographs of the laser melted samples are shown in Fig. 2. After LSM, the large equiaxed grains at or near the surface transformed to a fine grain network in the laser melted regions. The laser modified zone is referred to as melt pool. From Fig. 2a it is evident that a transition occurs in the grain morphology through the depth of the melt pool from equiaxed to columnar. As the laser energy density changes, the melt pool depth also changes. Further maximum depth of 152 µm was observed at an energy density of 17.5 J/mm^2 and a minimum depth of 102 µm was observed for the sample processed at 12.5 J/mm^2. Figure 3 shows the melt pool depth variation as a function of laser energy density (also shown individually in terms of laser power and velocity). The variation in the size of the melt pool can be attributed to the variations associated with the different cooling rates at different laser energy densities. The depth of the melt pool effectively influences the propagation of the corrosion front from the surface towards the substrate and thereby influencing the degradation rate [17].

Irrespective of the laser energy density, refinement of grains has occurred in all the LSM processed samples. Figure 2 shows the transformation of microstructure in the melt pool region. In region 1 (Fig. 2a) which is at or near the surface of the melt pool the microstructure exhibits fine grain structure with homogenous phase distribution (Fig. 2b). In this region, the grain size is in the range of 1–2 µm, which is ~98% less than as-cast grain size. In region 2 (Fig. 2a) which is near the bottom of the melt pool the microstructure exhibits columnar grains (Fig. 2c). Region 3 of Fig. 2a represents the overlapping region between successive melt pools. Region 4 of Fig. 2a can be referred to as heat-affected zone (HAZ).

EDS compositional analysis of the melt pool showed an enrichment of alloying elements (Gd, Nd, Zn) within the α-

Power (W)	Velocity (mm/s)	Energy density (J/mm^2)	Meltpool geometry (µm)
125	10	25	132±4
125	20	12.5	102± 4
175`	10	35	133±4
175	20	17.5	152±4
225	10	45	130±5
225	20	22.5	115±4

Fig. 3 Laser processing parameters and melt pool depth variation

Mg grain boundary with an increase in the laser energy density, as shown in Table 1. The formation and distribution of secondary phases are less likely to happen during casting because of the lower temperatures. When the laser beam is focused on the surface the temperature of the alloy increases

Table 1 EDS analysis of regions inside the Mg grains of LSM treated samples

Conditions	Weight percentage (wt%)			
	Mg	Zn	Gd	Nd
As-cast	97.3 ± 1	0.2 ± 0.2	1 ± 0.3	0.6 ± 0.3
12.5 J/mm^2	94.8 ± 0.5	4 ± 0.3	0.11 ± 0.4	0.88 ± 0.5
25 J/mm^2	83.2 ± 0.2	4.2 ± 0.5	5.1 ± 0.5	1.3 ± 0.3
45 J/mm^2	85.8 ± 0.3	5.8 ± 0.4	6.2 ± 0.5	2.2 ± 0.4

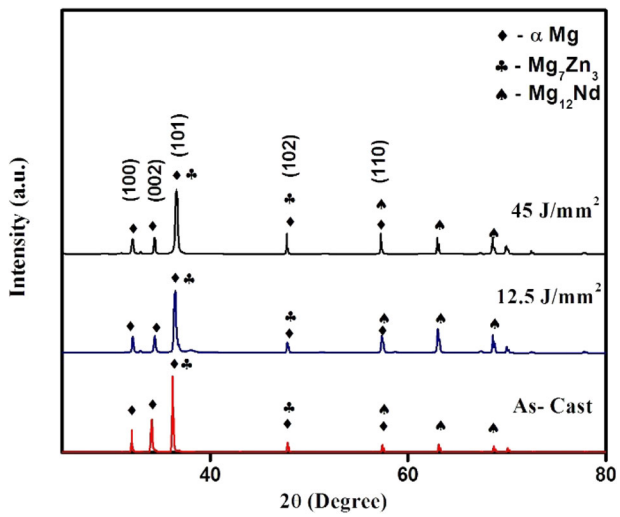

Fig. 4 Phase analysis of as-cast and LSM Mg–Zn–Gd–Nd alloy

rapidly to a temperature above the melting point of α-phase. In the liquid stage, the alloying elements start to diffuse into the matrix and thereby the final composition is enriched with Zn, Gd and Nd. When the laser beam moves away from the melt pool region the metal solidifies and reheating of this zone occurs again during the subsequent laser passes adjacent to this region. This can redistribute the secondary phases with some enrichment of alloying elements within the Mg matrix. The elevated concentration of solute elements could also be due to selective evaporation of Mg during LSM. As the energy density increases, the peak melt pool temperature increases and the rapid cooling rates associated with LSM further extends the solubility of the alloying elements in the Mg matrix leading to observed enrichment of solutes [13, 17], as shown in Table 1.

3.2 Phase analysis

XRD patterns of as-cast and LSM samples of Mg–Zn–Gd–Nd alloy are shown in Fig. 4. XRD patterns exhibit strong diffraction peaks at 32.19°, 34.4° and 36.63° indicating α-Mg phase. It was observed that the preferred orientation of the (101) plane decreased with laser melting. The diffraction peaks at 2θ = 40° to 80° show additional peaks with different relative intensities which strongly depend on the formation of secondary intermetallic phases (Mg_7Zn_3 and $Mg_{12}Nd$) (JCPDS reference code 03-065-2226 and 00-017-0401) due to rapid melting and solidification. Debye-Scherrer's formula [33] was also used to understand the variations in grain size of as-cast and LSM samples from the XRD spectra as given below.

Table 2 FWHM and grain size of the as-cast and LSM samples

Energy density	FWHM (°)	Grain size (nm)
As-cast	0.0960	87
12.5 J/mm^2	0.1771	47.2
45 J/mm^2	0.3050	27.42

$$D = \frac{0.9\lambda}{\beta \cos\theta}. \quad (5)$$

In this equation, 'D' is the grain size, 'β' is the full-width half maxima (FWHM) of the film at (101) plane, 'θ' is the Bragg's angle, and λ is the incident ray wavelength that is considered to be 0.154 nm for Cu-Kα radiation.

The calculated values are tabulated in Table 2. The grain size was observed to decrease with an increase in laser energy density implying peak broadening and lowering of peak intensity. This grain refinement can be attributed to the rapid heating and cooling that take place during the LSM [34] process. The enrichment of Zn and Nd (Table 1) in the α-Mg matrix were due to the Mg evaporation and dissolution of intermetallic components leading to the change in lattice constant during laser melting [35]. The decrease in the lattice constant of the α-Mg phase results in a small right shifting in diffraction peaks of laser melted samples [36].

3.3 Microhardness distribution

Figure 5 shows the hardness distribution of as-cast and LSM samples. Hardness measurements were carried out across the cross-section of the LSM zone (Fig. 5). The results reveal that there is a significant improvement (~1.3 times) in the hardness after LSM. The sample processed at 35 J/mm^2 exhibited a maximum hardness of 98 HV. As discussed earlier, the grain size in the LSM zone in the range of 1–2 µm. This grain refinement and uniform distribution of hardening phases lead to the improved hardness in all LSM samples. For better understanding indentation points in the samples are also represented in Fig. 5. The average hardness distribution is in the range of 85–90 HV for a sample processed at intermediate energy densities (17.5 J/mm^2, 22.5 J/mm^2 and 25 J/mm^2). Furthermore, the change in the rate of solidification at higher energy densities could presumably influence grain coarsening and thereby reducing the surface hardness [34, 37].

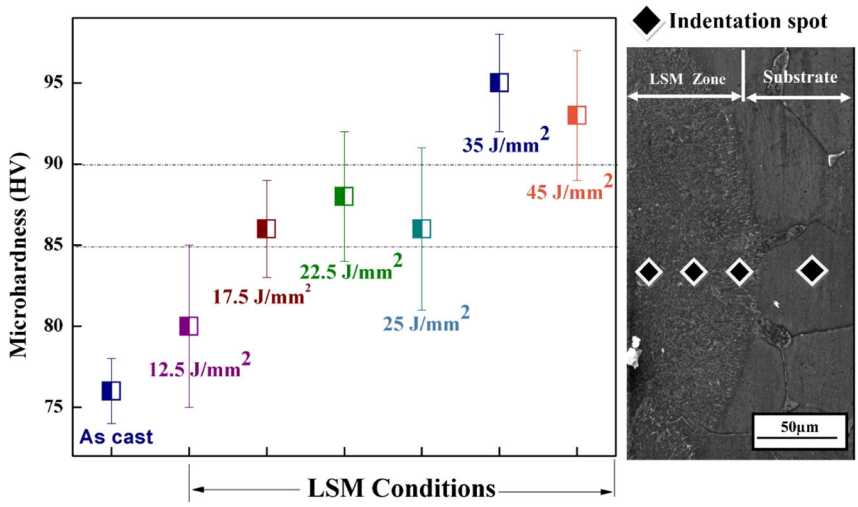

Fig. 5 Micro hardness distribution and cross-sectional indentation spots in the samples

Table 3 Comparison of surface energy and surface roughness results of LSM and LSM polished samples

	Laser melted samples		Laser melted and polished samples	
	Surface roughness (S_q) (µm)	Surface energy (mN/m)	Surface roughness (S_q) (µm)	Surface energy (mN/m)
As cast	1 ± 1	10 ± 5	1 ± 1	10 ± 5
12.5 J/mm^2	3.3 ± 1	36.1 ± 2	0.88 ± 0.1	37.5 ± 7
17.5 J/mm^2	6.3 ± 1	19.8 ± 3	1.14 ± 0.5	37.5 ± 7
22.5 J/mm^2	7 ± 2	21.9 ± 5	1.58 ± 0.8	35.7 ± 5
25 J/mm^2	9.4 ± 0.5	17.9 ± 8	1.04 ± 0.3	36.6 ± 6
35 J/mm^2	15.8 ± 1	17.3 ± 3	1.47 ± 0.5	35.7 ± 2
45 J/mm^2	16.8 ± 2	13.5 ± 4	1.2 ± 0.6	33.7 ± 4

3.4 Surface analysis of LSM specimens

Surface roughness is a key parameter to be monitored to control the surface wettability of the material after LSM. The average surface roughness (S_q) which is the main parameter to be measured for topography characterization is represented in Table 3. Increase in the energy density increases the surface roughness from 3.3 µm to 16.8 µm. Higher roughness values were observed in samples processed at higher energy densities especially at 35 and 45 J/mm^2. Intermediate energy densities (17.5 and 22.5 J/mm^2) did not show a significant variation in S_q value. This is because of they are effected with relatively similar hydrodynamic melt pressure. The measured surface topographical changes were mainly caused by the physics of hydrodynamic melt pool, recoil pressure and surface tension effects. The absorbed laser energy varies by the applied beam energy to the surface. The magnitude of the laser energy density affects heating, melting and vaporization of the metal surface. The evaporated vapour particle from the laser material interaction zone tries to condense back to the melt pool by inducing a recoil pressure [38]. This shock wave causes the ejection of liquid by hydrodynamic melt pool motion towards the edges of the melt pool. Further, the tangential stress exerted at the liquid crown due to the surface tension leaves a pronounced surface topography [35]. The higher energy density conditions (35 and 45 J/mm^2) are more pronouncedly effected with this higher magnitude of recoil pressure which in turn leads to higher surface roughness (15.8 and 16.8 µm, respectively). The profile of the surface has a significant influence on contact and adhesion of the cells once the material is in the in vivo condition.

The static sessile drop method was used to analyze the wettability of as-cast and LSM samples using DI water. The contact angles of different laser melted surfaces are shown in Fig. 6. The wetting ability of LSM samples is a direct reflection of surface energy, surface roughness, chemical composition and grain size [35]. However, it is difficult to explain which factor plays a predominant role on surface wettability. There is a quantitative way to correlate the surface energy with contact angle and surface roughness (Table 3 and Fig. 6). At lower energy densities (12.5–25 J/mm^2), the change in melting and vaporization rate aids in decreasing surface energy from 36.1 ± 2 mN/m to 17.9 ± 8 mN/m corresponding to an increase in contact angle from 72.2 ± 9° to 85.5 ± 7°, thereby indicating hydrophilic nature. It was found that when the contact angle increased the surface energy of the LSM alloy decreased. Moreover, the water wetting behaviour of sample surface changes to hydrophobic at 35 J/mm^2. Varying surface energy alters surface roughness profile thereby smoother surfaces could maximize surface energy [39]. The surface roughness (Sq) increased gradually from 6.3 ± 1 µm to 16.8 ± 2 µm with an increase in laser energy density. In surfaces processed at higher energy densities, water droplets

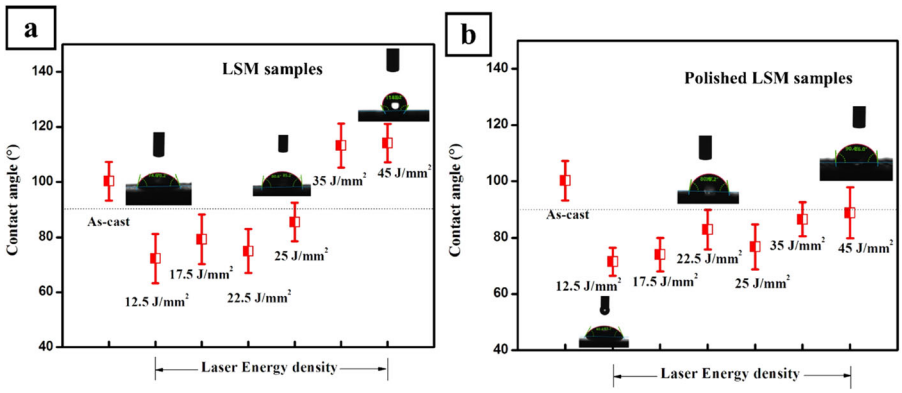

Fig. 6 Contact angle variation in **a** LSM **b** polished LSM samples with respect to the energy density and as-cast conditions

rest on an uneven surface with deeper valleys and taller peaks leading to reduce wetting [19].

In LSM polished samples, at lower energy density conditions effective wetting occurs due to larger grain size and smaller grain boundaries. At higher energy density conditions, the poor wetting behaviour can be attributed to the fine grain size and non-uniform chemical composition [35]. To study the feasibility of using LSM processed sample surfaces with minimum roughness in implant applications, the deeper valleys and taller peaks have been smoothened out from LSM samples with polishing. This enables them to attain uniform surface roughness (~Sa = 1 µm) to better understand their wetting behaviour. The surface energy and contact angle data for polished surfaces follow the same trend as unpolished surfaces (Table 2) which were discussed earlier. However, it is clearly evident from Table 2 and Fig. 6 that LSM polished samples show better wettability than unpolished LSM samples. This is mainly due to the lower contact angle values (from 70 to 90° as shown in Fig. 6b) as a result of compositional and microstructural changes due to LSM as all the samples have comparable surface roughness.

3.5 In vitro degradation studies

The degradation behaviour of as-cast and LSM Mg–Zn–Gd–Nd alloy was studied by the static immersion method, and the results are discussed here. Mg and its alloys undergo the dissolution primarily by the production of Mg^{2+} (anodic partial reaction) and hydrogen gas evolution (cathodic partial reaction) [40]. Therefore, to understand the degradation behaviour of as-cast and LSM sample, hydrogen evolution, Mg^{2+} ion release and weight loss methods were employed during and after the immersion of samples in HBSS.

Figure 7a represents the hydrogen evolution results. It is evident from the results that the trend is changing with the immersion time. It was observed that the initial release of hydrogen is linear to the immersion time. The maximum hydrogen evolution is observed for as-cast (without LSM) and 12.5 J/mm^2 LSM processed samples. The lower release of hydrogen was mainly observed for higher energy density processed samples (35 and 45 J/mm^2). The initial slope of the hydrogen evolution versus time graph was measured, and it is enlarged and represented in Fig. 7a.1. A high slope of 0.014 ml/cm^2/h was observed for as-cast and 12.5 J/mm^2 sample during the period of 80 h of immersion. During this period, the maximum amount of hydrogen production varied between 0.83 ml/cm^2 and 0.7 ml/cm^2 for as-cast and 12.5 J/mm^2 samples respectively. A minimum slope of 0.003 ml/cm^2/h was observed at 45 J/mm^2 and a maximum hydrogen release rate of 0.29 ml/cm^2. This value of hydrogen evolution is very lower than the maximum values of other samples. The intermediate slope values of 0.01 ml/cm^2/h, 0.006 ml/cm^2/h and 0.005 ml/cm^2/h were observed for 17.5 J/mm^2, 22.5 J/mm^2 and 25 J/mm^2, respectively. The amount of hydrogen evolved for LSM samples at higher energy density conditions was significantly lower than the untreated as-cast sample for the entire period of immersion studies, owing to their relatively good in vitro degradation resistance. The hydrogen evolution trend remains almost the same (especially for 45, 35, 22.5 J/mm^2 samples) after 100 hours of immersion indicating passive film formation. In samples processed at higher energy density conditions (45, 35 and 25 J/mm^2) the H_2 evolution trends are decreasing during the final hours of immersion suggesting the existence of the stable products on the surfaces. The final corrosion rate calculated from hydrogen evolution is represented in Fig. 8. Among all samples, the one processed at 45 J/mm^2 showed the lowest corrosion rate. A lower hydrogen production trend also corroborates these results.

The evolution of Mg^{2+} ions during the immersion of 180 h is shown in Fig. 7b. As observed with the hydrogen production trend, the Mg^{2+} release also varied linearly with immersion time. The slopes of the Mg^{2+} release versus time graph are enlarged at different time intervals (~20–80 and ~90–140) to understand the increment in the ion release and are represented in Fig. 7b.1, b.2. During the initial period, (Fig. 7b.1) the release of ions was drastic and a maximum

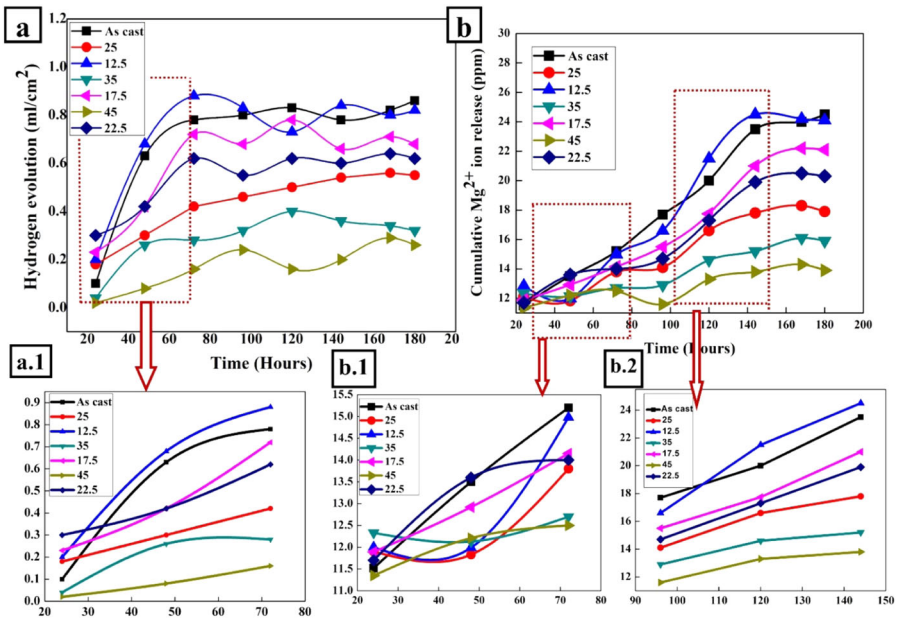

Fig. 7 **a** The hydrogen evolution trend (**a.1**) enlarged view **b** Mg^{2+} ion release (**b.1**), (**b.2**) enlarged views as a function of immersion time in HBSS

slope of 0.08 ppm/h, and 0.06 ppm/h were observed for 12.5 J/mm^2 and as-cast samples respectively. Similarly, these samples showed a maximum release of Mg^{2+} of about 24.5 ppm and 24 ppm for 12.5 J/mm^2 and as-cast samples respectively. During the initial period of immersion as-cast samples showed a higher Mg^{2+}release. But nearly after 120 h, the 12.5 J/mm^2 sample showed a higher slope of 0.16 ppm/h when compared to as-cast sample (0.12 ppm/h). The minimum concentration of Mg^{2+} in HBSS was observed to be 13.9 ppm and which is much less (almost 43%) than that of the as-cast sample. During the period of ~90–140 h, (Fig. 7b.2) there is a sharp increase in slope as compared to the initial stages of immersion. The abrupt changes in the ion release could be due to the local destruction of the passive film. During the same period, the slope at the higher energy density conditions was almost similar in magnitude, (0.047 ppm/h for 35 J/mm^2, 0.45 ppm/h for 45 J/mm^2). A maximum slope of 0.16 ppm/h was observed further 12.5 J/mm^2 LSM processed sample (Fig. 7b.2). The fluctuations in the trends at 12.5 J/mm^2 are mainly due to the defects caused due to low energy melting of the alloy. The release of Mg^{2+} ions gets stabilized after 140 h of immersion mainly for 17.5 J/mm^2, 22.5 J/mm^2 and 35 J/mm^2 samples. There is a small decrement in ion release at the same time for the 45 J/mm^2 and 25 J/mm^2 samples. The corrosion rate calculated from the Mg^{2+} release is also represented in the Fig. 8.

The corrosion rate calculated is using different ways is compared and represented in Fig. 8. The corrosion data shows that LSM improves corrosion resistance. Further, the corrosion rate trends from the three methods are in agreement with each other. The changes in the corrosion behaviour of the LSM specimen are due to [13, 16, 15]:

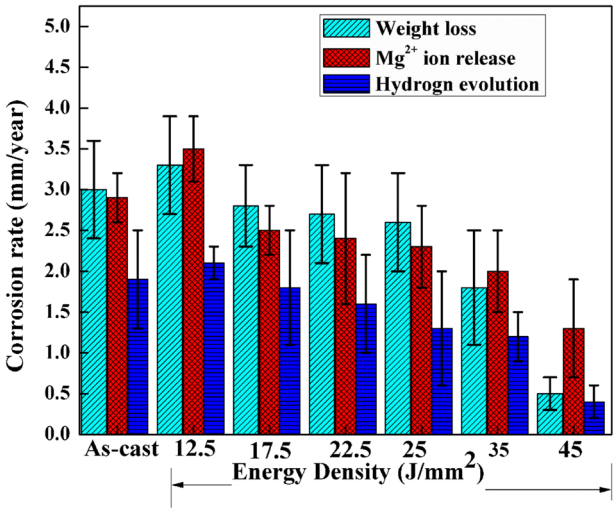

Fig. 8 Comparison of degradation rate obtained using different methods in samples polished after LSM

(a) modifications in the microstructure (b) changes in the composition, roughness [41] or residual stress [42] caused due to a high energy laser beam. The microstructure of as-cast and LSM samples were taken into account for understanding the corrosion characteristics. The secondary particles precipitated in the as-cast alloy were found to be Gd/Nd particles. These particles were dissolved partially which could be due to the high melting point of the Nd and Gd. Mg_{12} Nd, and T-phase (Mg_7Zn_3RE) particles were observed in these alloys and these precipitates are both large in size and are also non-uniformly distributed. Hence, the untreated alloy had undergone severe damage by the dissolution of the α-Mg matrix near to the secondary phase by galvanic couple formation. When the time of immersion increases,

the number of corrosion pits formed increased and they are also large in size. The LSM samples showed improved corrosion resistance due to grain refinement and uniform distribution of corrosion-resistant intermetallic phases such as $Mg_{12}Nd$ and Mg_7Zn_3 due to the rapid solidification.

Generally magnesium and its alloys are susceptible to micro-galvanic effect because of their relatively lower electrochemical potential than the impurities and secondary phases present in them [43]. Surface modification by laser surface melting (LSM) refines the grain size and redistributes the secondary phases within the matrix, which in turn enhances the mechanical and corrosion properties of Mg alloys. The main factors which influence corrosion of Mg alloys are grain refinement and the formation of additional protective layers due to active reaction with the environment [44]. Although the formation of corrosion products on the surface of Mg alloys improves the passivity, any cracks in these protecting layers, due to the tensile stresses generated within the oxide layer, can potentially accelerate corrosion. Argade et al. [45] suggested that the severity of cracking can be reduced in the materials with increase in grain boundary area. This can be achieved with LSM process via grain refinement. Therefore, the formation of more stable and adherent oxide layer on the present LSM surfaces would have decreased their corrosion rate. Secondary phases along the grain boundaries can act as a barrier to corrosion [43, 46]. Corrosion often initiates at the grain boundaries due to their relatively high energy and makes them anodic with respect to the grain interior. However, in LSM samples the uniform distribution of secondary phases with nobler potential around the refined α-phase grain region can decrease the anodic effects of grain boundaries and therefore decreases the corrosion rate. Similar role of β phase network ($Mg_{17}Al_{12}$) in the AZ31B system has been correlated with pitting corrosion after LSM [46].

Several studies reported the relationship between the grain size and corrosion rate of Mg alloys [29, 43, 47]. Typically, the grain boundaries which are considered as high-energy areas in the microstructure can lead to high corrosion rate due to the formation of galvanic couple between anodic grain boundary and cathodic grain interior. However, this trend is expected to change with ultra-fine grains such as those observed in the present work due to LSM and through which increase in grain boundary area can be achieved. The reduction in the corrosion rate due to ultra-fine grains in the LSM zone can be attributed to (1) accelerated passivation kinetics of the surface as a result of high amount of high-energy grain boundary area, and (2) reduction of the intensity of the galvanic couples (between grain boundary and interior). The closely spaced anodic-cathodic electrochemical cells lead to relatively more uniform corrosion and lower corrosion rate. In addition, the presence of rare earth elements (REE) in Mg also improves their corrosion behaviour by formation of protective surface layer. Overall, it can be said that both LSM induced microstructural changes and the REE addition are responsible for observed improvement in the corrosion performance of present LSM processed Mg–Zn–Gd–Nd alloy.

Studies [48, 49, 44] have shown the combined influence of grain refinement, uniform distribution of secondary phase and effective passive layer formation enhances the corrosion resistance in laser melted samples. $Mg_{12}Nd$ phase present in the alloy has slightly higher corrosion potential than Mg [9]. Therefore, enrichment and uniform distribution of this phase after LSM lead to a positive influence on degradation properties [46]. Reduced corrosion resistance was observed in the 12.5 J/mm^2 when compared to as-cast alloy. This higher corrosion rate can be attributed to the solidification cracks and partially melted phases in the melt pool region. This leads to a further increase in galvanic cell formation resulting in significant corrosion pits formation on the exposed surface (Fig. 10a). A minimum corrosion rate of 0.5 mm/year was found for 45 J/mm^2 sample which is 83% higher than the untreated as-cast sample. A very small difference in the value of corrosion rate was observed in samples processed at low energy density conditions (12.5, 17.5 and 22.5 J/mm^2 which are in the order of 3.3, 2.8 and 2.7 mm/year, respectively). The drastic reduction of corrosion rate is mainly observed at higher energy densities conditions (predominantly at 35 and 45 J/mm^2). It was observed that the solid solubility of Gd and Nd elements after LSM was improved (Table 1). This enrichment reduces the corrosion susceptibility of α-Mg by reducing the potential difference between the phases [36].

3.6 Characterization of corrosion damage

The depth of corrosion damage and its mechanism after 180 h of immersion is shown in the cross-sectional SEM images of the samples (Fig. 9). Figure 9a shows the as-cast sample, wherein the corroded area is deeply enlarged to the interior and a larger pit is formed leaving isolated grains (dashed square) across the region. The LSM processed sample at 12.5 J/mm^2 shows severe damage. The melt zone is completely dissolved into the solution and thereby forming a boat like pit (melt zone pit). An island like melt region (enlarged view in Fig. 9b) was also observed after the corrosion attack on the surface. The potential difference formed between the solidification crack (defects) and the melt zone leads to the formation of a corrosion site, and this will start to propagate rapidly towards the substrate region [17]. The Difference in the cathode to anode ratio between the melt zone boundary and the substrate further promotes the localized corrosion combined with a number of corrosion pits [50]. The formation of smaller pits in the melt zone was observed in Fig. 9c, wherein the sample was processed

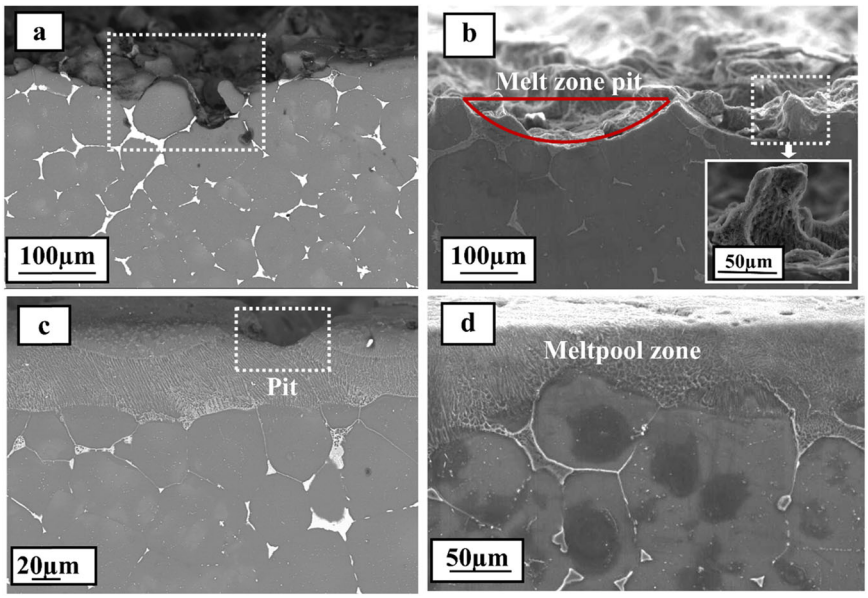

Fig. 9 Cross-sectional SEM images of **a** as-cast **b** 12.5 J/mm^2 **c** 35 J/mm^2 **d** 45 J/mm^2 samples after 180 h of immersion in HBSS

at 35 J/mm^2. This is an intermediate zone where the corrosion progression is limited. The propagation and the life of the sample depend on the microstructure and depth of the refined zone by the LSM treatment. The maximum depth of 152 µm (Fig. 3) was observed in 35 J/mm^2 samples and is expected to give longer immersion life in HBSS. A more pronounced melt zone with a continuous network of fine cells was observed in the 45 J/mm^2 sample (Fig. 9d). Inspite of this, there is no depletion of the exposed surface after 180 h of immersion in HBSS.

The exposed area of the surface to the HBSS is now accounted in the study, and the SEM images are represented in Fig. 10. The degradation characteristics of the LSM samples exhibit pitting mode of corrosion combined with the modest dissolution of the modified secondary phases [4]. The surface of the as-cast sample shows (Fig. 10a) deep pits at the eutectic compound ($Mg_{12}Nd$) due to the micro galvanic cell formation between this cathodic phase and α-anodic matrix. As a consequence of this galvanic cell formation, the corrosion was spread out to the grain boundary region and dissolved the eutectic phase. Finally, corrosion deeply damaged the matrix phase leaving deeper and random broader pits (arrow 1 and 2 in Fig. 10a). A number of tiny pits are formed and spread over the matrix region, and it is enlarged and represented in Fig. 10a (arrow 3). The corrosion was more advanced on the surface of the lower energy density (12.5 J/mm^2) processed sample. After prolonged immersion, different areas appeared at the exposed surface of 12.5 J/mm^2 sample. Some areas were unaffected and seen as honeycomb-like structure (Fig. 10b arrow 1) in the LSM zone. There were areas where complete dissolution of the modified region was observed. It is well evident (Fig. 10b arrow 2) that the substrate becomes visible because of the depletion of the laser modified region. Figure 10c indicates the surface of 35 J/mm^2 LSM sample with laser track seen after the immersion. The more pronounced surface track seen on the alloy signifies less corrosion damage. The enlarged view shows the presence of the passive film retained on the surface even after removing the corrosion products. The EDS results of these products reveal the formation of protective $Mg(OH)_2$ phase. The degree of attack is considerably lower in 45 J/mm^2 sample, and it is represented in Fig. 10d. The formation of smaller pits was observed in this sample and their enlarged view is shown in Fig. 10d (arrow 1).

Protective film generation and its involvement in the protection of metallic surfaces after long term immersion in HBSS were studied. The surface corrosion products were carefully removed and its features were analyzed (Fig. 11). During the initial stages of immersion, oxidant from the solution initiates the corrosion process at the metal-solution interface. The continued dissolution of the protective layer was followed by oxidation and precipitation of corrosion products [51]. The degradation products progressively became thick, and are difficult to remove from the LSM treated surface. Morphologically different products were formed at the surface at different phases of immersion. After a certain period of immersion, interactive diffusion of the elements from the substrate and HBSS is ceased with increased carbonate/phosphate or hydroxide layer formation. During the initial stage of immersion, the Mg^{2+} ions are liberated from the surface through the porous layer by capillary action to the solution metal interface. Similarly, various ions from the HBSS propagate in the opposite direction and reacted with the ions present at the metal surface and new products get deposited and they densified.

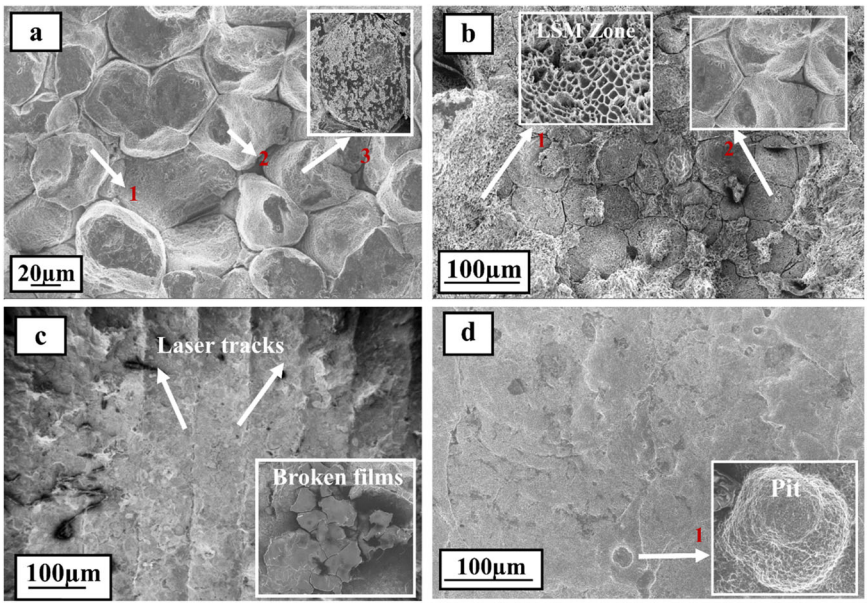

Fig. 10 Surface morphology of **a** as-cast **b** 12.5 J/mm^2 **c** 35 J/mm^2 **d** 45 J/mm^2 samples after 180 h of immersion in HBSS taken in SEM

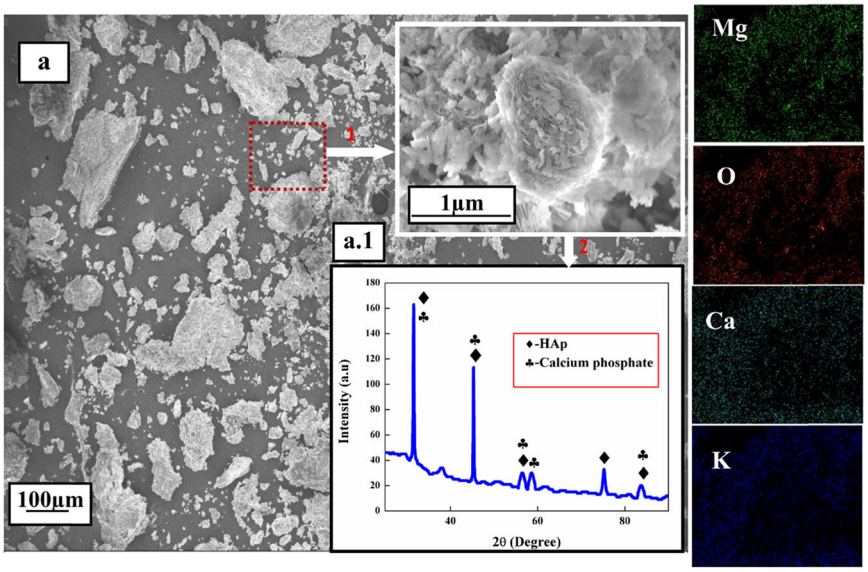

Fig. 11 Surface product analysis by SEM + EDS Mapping and XRD

The formation of the protective/passive film further lowers the degradation rate [44]. It is observed that the bright and randomly distributed flakes (Fig. 11a) consist of Ca, O, P, Mg and Cl. EDS mapping result of these products shows the distribution intensity of these elements. The enlarged SEM view in Fig. 11 (arrow 1) shows the dense cluster with calcium and phosphate-rich phases similar to apatite formation. It indicates that $H_2PO_4^-$, HPO_4^{2-}, HPO_4 and OH^- ions from the HBSS reacted with one other and formed the products effectively on the exposed surface [52]. The XRD results (Fig. 11a.1) show that the degradation products are $Ca_3(PO_4)_2$ (calcium phosphate) and $Ca_5(PO_4)_3OH$ (Hydroxyapatite). The major peaks indexed are $2\theta = 31.5°$, 45.3°, 56°, 75° and 83.4° for HAp (JCPDS 00-024-0033), and it is a bit dominant on the surface. Similarly, calcium phosphate is also suitably indexed (JCPDS 00-009-0348). HAp is an essential element of the human bone, and the deposition of HAp accelerates bone tissue growth. Consequently, the formation of products support the in vivo bone activity of the material and the ratio of Ca/P (1.7) is well above the actual stoichiometric ratio of Ca/P (1.67) for better apatite formation [53]. The presence of Cl^- from the corrosive media transforms the $Mg(OH)_2$ passive film into soluble $MgCl_2$ and changes the dynamic balance of degradation during the period of immersion [54]. FTIR spectra (Fig. 12) of the corrosion products also confirm the precipitation of

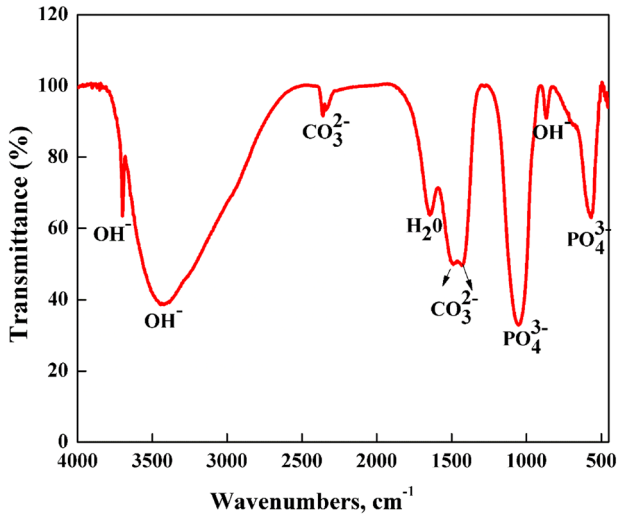

Fig. 12 FTIR Spectra of corrosion products extracted after 180 h of immersion in HBSS

phosphate, carbonate and hydroxide compounds. The intensity band of PO_4^{3-} lies in the wavenumber range of 563 and 1049 cm^{-1}. This P–O bond is an indication of hydroxyapatite in crystalline form. The obtained OH^- band intensity at 3430 cm^{-1} is relatively wider than the band observed at 3696 cm^{-1}. CO_3^{2-} group formed a weak peak at 2351 cm^{-1} and a comparatively strong peak was observed between 1418 and 1490 cm^{-1}. During the period of immersion, the stable calcium phosphate and calcium carbonate precipitate formation might restrict further corrosion attack on the surface of the samples [55]. One peak of water (H_2O) band was observed at 1642 cm^{-1}. The obtained intensity bands were correlated with the reported studies [56, 57].

4 Conclusions

The following conclusions can be drawn from the study of laser surface melted Mg–Zn-Gd–Nd alloy:

(1) The microstructure of the melted region consisted of fine equiaxed grains of α-Mg phase. Grain refinement of ~96 % occurred in the melt zone due to rapid solidification associated with LSM.
(2) The microhardness of the laser melted region increased which is attributed to the grain refinement. Maximum hardness of 95 HV was recorded with the samples processed at 35 J/mm^2 which is 25% higher compared to as-cast alloy.
(3) LSM increased the surface roughness of the sample which appears to decrease the surface energy. However, improved hydrophilic behaviour was obtained after surface polishing the samples. Contact angle results indicate that the surface roughness, grain size and chemical composition have a strong influence on the surface wettability of this alloy.
(4) The improved corrosion resistance of the alloy due to LSM was confirmed by three different measurement techniques. Our results showed a maximum improvement of 83% in the corrosion resistance of samples processed at a laser energy density of 45 J/mm^2 when compared to as-cast alloy.

Acknowledgements Authors would like to thank Dr Anandhan Srinivasan and his group from the Metallurgical and Materials Engineering department and the Chemical Engineering department at the National Institute of Technology, Karnataka for providing access to FTIR and Atomic Absorption Spectroscopy facilities respectively.

Compliance with ethical standards

Conflict of interest The authors declare that they have no conflict of interest.

Publisher's note Springer Nature remains neutral with regard to jurisdictional claims in published maps and institutional affiliations.

References

1. Witte F. Reprint of: the history of biodegradable magnesium implants: a review. Acta Biomater 2015;23:S28–40.
2. Chen Y, Xu Z, Smith C, Sankar J. Recent advances on the development of magnesium alloys for biodegradable implants. Acta Biomater. 2014;10:4561–73.
3. Gu XN, Zheng W, Cheng Y, Zheng YF. A study on alkaline heat treated Mg-Ca alloy for the control of the biocorrosion rate. Acta Biomater. 2009;5:2790–9.
4. Chang JW, Fu PH, Guo XW, Peng LM, Ding WJ. The effects of heat treatment and zirconium on the corrosion behaviour of Mg-3Nd-0.2Zn-0.4Zr (wt.%) alloy. Corros Sci. 2007;49:2612–27.
5. Feyerabend F, Fischer J, Holtz J, Witte F, Willumeit R, Drücker H, et al. Evaluation of short-term effects of rare earth and other elements used in magnesium alloys on primary cells and cell lines. Acta Biomater. 2010;6:1834–42.
6. Srinivasan A, Huang Y, Mendis CL, Blawert C, Kainer KU, Hort N. Investigations on microstructures, mechanical and corrosion properties of Mg-Gd-Zn alloys. Mater Sci Eng A. 2014;595:224–34.
7. Zong Y, Yuan G, Zhang X, Mao L, Niu J, Ding W. Comparison of biodegradable behaviors of AZ31 and Mg – Nd – Zn – Zr alloys in Hank' s physiological solution. Mater Sci Eng B. 2012;177:395–401.
8. Niu J, Yuan G, Liao Y, Mao L, Zhang J, Wang Y, et al. Enhanced biocorrosion resistance and biocompatibility of degradable Mg-Nd-Zn-Zr alloy by brushite coating. Mater Sci Eng C. 2013;33:4833–41.
9. Zhang X, Yuan G, Mao L, Niu J, Fu P, Ding W. Effects of extrusion and heat treatment on the mechanical properties and biocorrosion behaviors of a Mg-Nd-Zn-Zr alloy. J Mech Behav Biomed Mater. 2012;7:77–86.
10. Hornberger H, Virtanen S, Boccaccini a R. Biomedical coatings on magnesium alloys—a review. Acta Biomater. 2012;8:2442–55.
11. Gray JE, Luan B. Protective coatings on magnesium and its alloys - a critical review. J Alloys Compd. 2002;336:88–113.

12. Kusinski J, Kac S, Kopia A, Radziszewska A, Rozmus-Górnikowska M, Major B. et al. Laser modification of the materials surface layer-a review paper. Bull Polish Acad Sci Tech Sci. 2012;60:711–28.
13. Mondal AK, Kumar S, Blawert C, Dahotre NB. Effect of laser surface treatment on corrosion and wear resistance of ACM720 Mg alloy. Surf Coat Technol. 2008;202:3187–98.
14. Khalfaoui W, Valerio E, Masse JE, Autric M. Excimer laser treatment of ZE41 magnesium alloy for corrosion resistance and microhardness improvement. Opt Lasers Eng. 2010;48:926–31.
15. Abbas G, Liu Z, Skeldon P. Corrosion behaviour of laser-melted magnesium alloys. Appl Surf Sci. 2005;247:347–53.
16. Coy AE, Viejo F, Liu Z, Skeldon P, Thompson GE. Effect of excimer laser surface melting on the microstructure and corrosion performance of the die cast AZ91D magnesium alloy. Corros Sci. 2010;52:387–97.
17. Rakesh KR, Bontha S, Ramesh MR, Arya SB, Das M. Laser surface modification of Mg-Zn-Gd alloy: microstructural, wettability and in vitro degradation aspects Laser surface modi fi cation of Mg-Zn-Gd alloy: microstructural, wettability and in vitro degradation aspects. Mater Res Express. 2018;5:126502.
18. Bontha KRR. S, M.R. R, Das M, Balla VK. Laser surface melting of Mg-Zn-Dy alloy for better wettability and corrosion resistance for biodegradable implant applications. Appl Surf Sci. 2019;480:70–82. https://doi.org/10.1016/j.apsusc.2019.02.167.
19. Rosales-Leal JI, Rodríguez-Valverde MA, Mazzaglia G, Ramón-Torregrosa PJ, Díaz-Rodríguez L, García-Martínez O, et al. Effect of roughness, wettability and morphology of engineered titanium surfaces on osteoblast-like cell adhesion. Colloids Surf A Physicochem Eng Asp. 2010;365:222–9.
20. Dahotre SN, Vora HD, Rajamure RS, Huang L, Banerjee R, He W, et al. Laser induced Nitrogen enhanced Titanium surfaces for improved osseo-integration. Ann Biomed Eng. 2014;42:50–61.
21. Demir AG, Furlan V, Lecis N, Previtali B. Laser surface structuring of AZ31 Mg alloy for controlled wettability. Biointerphases. 2014;9:029009.
22. Kottuparambil RR, Bontha S, Rangarasaiah RM. Effect of zinc and rare-earth element addition on mechanical, corrosion, and biological properties of magnesium. J Mater Res. 2018;33:3466–78.
23. Marattukalam JJ, Kumar A, Datta S, Das M, Krishna V, Bontha S, et al. Microstructure and corrosion behavior of laser processed NiTi alloy. Mater Sci Eng C. 2015;57:309–13.
24. Owens DK, Wendt RC. Estimation of the surface free energy of polymers. J Appl Polym Sci. 1969;13:1741–7.
25. Song G, Atrens A, StJohn D. An hydrogen evolution method for the estimation of the corrosion rate of magnesium alloys. Magnes Technol. 2001;2013:254–62.
26. Shi Z, Liu M, Atrens A. Measurement of the corrosion rate of magnesium alloys using Tafel extrapolation. Corros Sci. 2010;52:579–88.
27. Zainal Abidin NI, Rolfe B, Owen H, Malisano J, Martin D, Hofstetter J, et al. The in vivo and in vitro corrosion of high-purity magnesium and magnesium alloys WZ21 and AZ91. Corros Sci. 2013;75:354–66.
28. Atrens A, Liu M, Zainal Abidin NI. Corrosion mechanism applicable to biodegradable magnesium implants. Mater Sci Eng B Solid-State Mater Adv Technol. 2011;176:1609–36.
29. Atrens A, Song G, Cao F, Shi Z, Bowen PK. Advances in Mg corrosion and research suggestions. J Magnes Alloy. 2013;1:177–200.
30. Cor E. Standard practice for laboratory immersion corrosion testing of metals 1. Corrosion. 2004;72:1–8.
31. Neil WC, Forsyth M, Howlett PC, Hutchinson CR, Hinton BRW. Corrosion of magnesium alloy ZE41–The role of microstructural features. Corros Sci. 2009;51:387–94.
32. Gui Z, Kang Z, Li Y. Evolution of the microstructure and fracture characteristics of a Mg- Nd-Zn-Zr-Mn alloy through heat treatment and extrusion. J Alloys Compd. 2018;68:4.
33. Ozdemir R, Karahan IH. Grain size calculation of Cu-Zn alloys using genetic programming; an alternative for Scherer's formula. J Optoelectron Adv Mater. 2015;17:14–26.
34. Dutta J, Arun M, Manna SK. Laser surface melting of AISI 316L stainless steel for bio-implant application. Proc Natl Acad Sci India Sect A Phys Sci. 2018;80:387–403.
35. Ho Y-H, Vora HD, Dahotre NB. Laser surface modification of AZ31BMg alloy for bio-wettability. J Biomater Appl. 2015;29:915–28.
36. Liu C, Liang J, Zhou J, Wang L, Li Q. Effect of laser surface melting on microstructure and corrosion characteristics of AM60B magnesium alloy. Appl Surf Sci. 2015;343:133–40.
37. Krishna V, Das M, Bose S, Ram GDJ, Manna I. Laser surface modification of 316 L stainless steel with bioactive hydroxyapatite. Mater Sci Eng C. 2013;33:4594–8.
38. Vora HD, Santhanakrishnan S, Harimkar SP, Boetcher SKS, Dahotre NB. One-dimensional multipulse laser machining of structural alumina: evolution of surface topography. Int J Adv Manuf Technol. 2013;68:69–83.
39. Zhu X, Chen J, Scheideler L, Reichl R, Geis-gerstorfer J. Effects of topography and composition of titanium surface oxides on osteoblast responses. Biomaterials. 2004;25:4087–103.
40. Thomas S, Medhekar NV, Frankel GS, Birbilis N. Corrosion mechanism and hydrogen evolution on Mg. Curr Opin Solid State Mater Sci. 2015;19:85–94.
41. Walter R, Kannan MB. Influence of surface roughness on the corrosion behaviour of magnesium alloy. Mater Des. 2011;32:2350–4.
42. Kouadri A, Barrallier L. Study of mechanical properties of AZ91 magnesium alloy welded by laser process taking into account the anisotropy microhardness and residual stresses by X-ray diffraction. Metall Mater Trans A Phys Metall Mater Sci. 2011;42:1815–26.
43. Esmaily M, Svensson JE, Fajardo S, Birbilis N, Frankel GS, Virtanen S, et al. Fundamentals and advances in magnesium alloy corrosion. Prog Mater Sci. 2017;89:92–193. https://doi.org/10.1016/j.pmatsci.2017.04.011.
44. Ho YH, Joshi SS, Wu TC, Hung CM, Ho NJ, Dahotre NB. In-vitro bio-corrosion behavior of friction stir additively manufactured AZ31B magnesium alloy-hydroxyapatite composites. Mater Sci Eng C. 2020;109:110632 https://doi.org/10.1016/j.msec.2020.110632.
45. Argade GR, Panigrahi SK, Mishra RS. Effects of grain size on the corrosion resistance of wrought magnesium alloys containing neodymium. Corros Sci. 2012;58:145–51. https://doi.org/10.1016/j.corsci.2012.01.021.
46. Wu TC, Ho YH, Joshi SS, Rajamure RS, Dahotre NB. Microstructure and corrosion behavior of laser surface-treated AZ31B Mg bio-implant material. Lasers Med Sci. 2017;32:797–803.
47. Birbilis N, Ralston KD, Virtanen S, Fraser HL, Davies CHJ. Grain character influences on corrosion of ECAPed pure magnesium. Corros Eng Sci Technol. 2010;45:224–30.
48. Alvarez-Lopez M, Pereda MD, Del Valle JA, Fernandez-Lorenzo M, Garcia-Alonso MC, Ruano OA, et al. Corrosion behaviour of AZ31 magnesium alloy with different grain sizes in simulated biological fluids. Acta Biomater. 2010;6:1763–71.
49. Ben Hamu G, Eliezer D, Wagner L. The relation between severe plastic deformation microstructure and corrosion behavior of AZ31 magnesium alloy. J Alloy Compd. 2009;468:222–9.
50. Manne B, Thiruvayapati H, Bontha S, Motagondanahalli Rangarasaiah R, Das M, Balla VK. Surface design of Mg-Zn alloy temporary orthopaedic implants: tailoring wettability and

biodegradability using laser surface melting. Surf Coatings Technol. 2018;347:337–49.
51. Sikora-Jasinska M, Chevallier P, Turgeon S, Paternoster C, Mostaed E, Vedani M, et al. Long-term in vitro degradation behaviour of Fe and Fe/Mg2Si composites for biodegradable implant applications. RSC Adv. 2018;8:9627–39.
52. Zhang X, Yuan G, Mao L, Niu J, Fu P, Ding W. Effects of extrusion and heat treatment on the mechanical properties and biocorrosion behaviors of a Mg–Nd–Zn–Zr alloy. J Mech Behav Biomed Mater. 2012;7:77–86.
53. Yang H, Xia K, Wang T, Niu J, Song Y, Xiong Z, et al. Growth, in vitro biodegradation and cytocompatibility properties of nano-hydroxyapatite coatings on biodegradable magnesium alloys. J Alloys Compd. 2016;672:366–73.
54. Song Y, Shan D, Chen R, Zhang F, Han EH. Biodegradable behaviors of AZ31 magnesium alloy in simulated body fluid. Mater Sci Eng C. 2009;29:1039–45.
55. Aboudzadeh N, Dehghanian C, Shokrgozar MA. In vitro degradation and cytotoxicity of Mg-5Zn-0.3Ca/nHA biocomposites prepared by powder metallurgy. Trans Nonferrous Met Soc China. 2018;28:1745–54.
56. Prekajski M, Mirković M, Todorović B, Matković A, Marinović-Cincović M, Luković J, et al. Ouzo effect-New simple nanoemulsion method for synthesis of strontium hydroxyapatite nanospheres. J Eur Ceram Soc. 2016;36:1293–8.
57. Jebri S, Boughzala H, Bechrifa A, Jemal M. Structural analysis and thermochemistry of “A” type phosphostrontium carbonate hydroxyapatites. J Therm Anal Calorim. 2012;107:963–72.